Seismic Structure of the Mantle Beneath the Southwestern Pacific

by

Liangjun Chen

B.S., Geophysics (1995)
Peking University

Submitted to the Department of Earth, Atmospheric, and Planetary Sciences
in Partial Fulfillment of the Requirements for the Degree of
Master of Science in Earth and Planetary Sciences

at the

Massachusetts Institute of Technology
September 2001

Signature of Author .....

Department of Earth, Atmospheric, and Planetary Sciences
July 31, 2001

Certified by .....

Thomas H. Jordan
Professor
hesis Supervisor

Accepted by .....

Ronald G. Prinn
Department Head

Seismic Structure of the Mantle Beneath the Southwestern Pacific

by

Liangjun Chen

Submitted to the Department of Earth, Atmospheric, and Planetary Sciences
in Partial Fulfillment of the Requirements for the Degree of
Master of Science in Earth and Planetary Sciences

Abstract

We jointly invert 1396 frequency-dependent travel times of turning and surface waves such as *S*, *sS*, *SS*, *sSS*, *SSS*, *Sa*, R_1, and G_1, together with 82 travel times of multiple *ScS* waves, to obtain a high-resolution, two-dimensional (2-D) vertical tomogram for the corridor between the Ryukyu subduction zone and Hawaii, which traverses the Hawaiian Swell between Midway and Oahu. The data analysis, inversion procedure, and parameterization are similar to our previous study along the Tonga-Hawaii corridor [*Katzman et al.*, 1998], but in this study we add corrections to the measurements that account for the crustal heterogeneity and topography along the path. The model parameters include shear-speed variations throughout the mantle, perturbations to shear-wave radial anisotropy in the uppermost mantle, and the topographies of the 410- and 660-km discontinuities. The model we obtained, which is well resolved in the upper mantle, exhibits high shear speeds at shallow depths and low speeds in the transition zone beneath the Pacific part of the corridor, with the lowest shear speed within a distinct upper-mantle anomaly at the depth of 200-400km near the Hawaiian Swell. Furthermore, we inverted the data from individual source arrays in New Hebrides, Solomon, and Mariana Island for two-dimensional vertical tomograms of mantle structure using the same technique as the Ryukyu-Hawaii corridor. The 2-D tomograms for these corridors were generally consistent with previous tomographic results, although they show upper-mantle features that are smaller in scale and larger amplitude than published global models. We then inverted the entire data set from all corridors for a 3-D model of the southwestern Pacific upper mantle. At low wavenumbers, this regional model is consistent with large-scale features found from global tomography. However, our model displays greater lateral heterogeneity in both isotropic and anisotropic structure than the global models, especially in the 200-400 km depth range, which can be attributed to the better resolution of small-scale features by our data set. Fast and slow anomalies in isotropic shear speed are observed in the upper mantle, suggesting a complex 3-D mantle flow in the southwestern Pacific upper mantle.

Thesis Supervisor: Thomas H. Jordan
Title: Professor

Contents

Chapter 1

Introduction

The three-dimensional (3-D) images of deep Earth structure provided by seismic tomography have placed strong constraints on the dynamics of the Earth's mantle [e.g., *Hager and Clayton*, 1989; *Forte et al.*, 1993; *Phipps Morgan and Shearer*, 1993; *Puster and Jordan*, 1997]. The resolution of these images has improved remarkably over the last decade, particularly for areas with high concentration of earthquakes and stations. In recent years, the regional surface-wave studies and high-resolution global studies have begun to elucidate interesting features, e.g., the normal seismic velocities obtained from dispersion of Rayleigh waves between Midway and Oahu [*Woods and Okal*, 1996]; the unique shear-wave anisotropy of the Pacific upper mantle [*Ekström and Dziewonski*, 1998]. Unfortunately, the resolving power of these studies decreases substantially for the ocean, particularly in the upper mantle far away from the sources and receivers. As a result, the upper-mantle structure beneath the Pacific Ocean has been constrained mostly by regional 1-D models [*Regan and Anderson*, 1984; *Nishimura and Forsyth*, 1989; *Gaherty et al.*, 1996] and by global tomographic studies [e.g., *Woodhouse and Dziewonski*, 1984; *Zhang and Tanimoto*, 1993; *Su et al.*, 1994; *Li and Romanowicz*, 1996; *Masters et al.*, 1996; *van der Hilst et al.*, 1997].

Structure of the oceanic upper mantle is interesting from a dynamic point of view, e.g., heterogeneities associated with small-scale convection and chemical variations. The structure in the vertical plane of the Tonga-Hawaii corridor, an oceanic region where previous knowledge of mantle heterogeneity has been limited because of the lack of stations and its distance from source regions, was recently studied by *Katzman et al.* [1998] (here after referred to as Paper I). In that paper, a high-resolution vertical tomogram for the Tonga-Hawaii corridor was obtained by jointly inverting frequency-dependent travel-time residuals of three-component turning and surface waves together with travel times of *ScS* reverberations. The resulting image revealed a well-resolved pattern of shear-speed highs and lows with an upper-mantle thickness; in particular, it

showed that a high shear velocity underlies each of the three northwest-trending geoid swells downstream from the hotspots of the Society, Marquesas, and Hawaii islands.

In this paper, we apply the tomographic methodology of Paper I to the Ryukyu-Hawaii corridor. This method uses the generalized seismological data functionals (GSDF) of *Gee and Jordan* [1992] to extract a large set of frequency-dependent travel times from shear-dominant wavegroups that include *S*, *sS*, *sSS*, *SSS*, *Sa*, R_1, and G_1. Using the 2-D Fréchet-kernel formulation of *Zhao and Jordan* [1998], we jointly invert these data together with a small set of multiple *ScS* times for a composite image for the vertical plane of the corridor. The resulting model, named RH2, is substantiated by a suite of resolution tests and by a series of full and partial data-set inversions. It reveals high shear speed in the shallow mantle in the Pacific part of the corridor and low shear speed in the transition zone, with the lowest shear speed within an upper-mantle anomaly at a depth of 200-400km beneath the Hawaiian Swell. There is also a strong contrast between the western Pacific Ocean and the Philippine Sea, with the latter exhibiting a very slow anomaly in the lithosphere and uppermost mantle, and a fast anomaly in the transition zone. We also apply the same methodology to the Mariana, Solomon, and Noumea-Hawaii corridors. The resulting models, named MH1, SH1, and NH1, are generally consistent with previous tomographic results, although they show upper-mantle features that are smaller in scale and larger amplitude than published global models. We then inverted the entire data set from all corridors for a 3-D model of the southwestern Pacific upper mantle. Our tomographic results for the southwestern Pacific indicate that the upper mantle in this region is chemically heterogeneous and dynamically active.

Chapter 2

Seismic Structure of the Mantle Along the Ryukyu - Hawaii Corridor

2.1 Reference Model and Attenuation Structure

Despite the tectonic heterogeneity of the Ryukyu-Hawaii corridor, which traverses two plates and a hotspot swell and crosses two subduction zones, the combined velocity structure of PA5 for the upper mantle [*Gaherty et al.*, 1996] and PREM [*Dziewonski and Anderson*, 1981] for the lower mantle appears to be an acceptable reference model (Fig. 2a). However, the attenuation structure of PA5 (Fig. 2b) does not provide a good representation for the Ryukyu-Hawaii corridor. Although the amplitudes of the synthetic body waves computed by this model are comparable to the observed ones, the synthetic surface-wave amplitudes, especially those of the Rayleigh waves traversing from Izu-Bonin to Oahu, are consistently and significantly lower than those in the data (Fig. 2d). We modified the attenuation structure by increasing the Q significantly in the lid (including the crust) and in the low-velocity zone and decreasing it only slightly in the lower part of the upper mantle (Fig. 2c), which fit the amplitudes of the surface waves without corrupting of the turning waves from either shallow- or deep-focus events (Fig. 2d). The resulting model, PA5', has slightly higher Q values for the upper mantle and the whole-mantle average than PA5 for the Tonga-Hawaii corridor, in agreement with the *ScS*-attenuation studies of the western and central Pacific [*Sipkin and Jordan*, 1980].

2.2 Multiple-*ScS* Data

Using the cross-correlation procedure described in Paper I, we measured the travel times of 82 multiple *ScS* waves on the transverse components of 13 seismograms. Of these seismograms, 10 were recorded at KIP and HON, both on Oahu, from 8 Izu-Bonin (55° <

$\Delta < 58°$), one Ryukyu ($\Delta = 75°$), and one Hawaiian ($\Delta = 5°$) earthquakes. These data were complemented by additional *ScS* travel times measured on 3 seismograms recorded at TATO, on Taiwan, from 3 Izu-Bonin events ($16° < \Delta < 17°$). For the 1973 Hawaiian event, which was also used in our Tonga-Hawaii study, the focal mechanism was taken from *Butler* [1982]. For all the other events, we used the Harvard CMT solutions. The events were of moderate size ($5.9 < M_W < 7.4$), with hypocentral depths of 166 to 523 km except for two shallow-focus events. The horizontal components of the recorded seismograms were rotated, and the transverse components were deconvolved using a damped-least-squares algorithm. This was followed by filtering with a zero-phase Hanning taper having a corner and a maximum frequency at 40 and 60 mHz, respectively.

2.3 Surface- and Body-Wave Data

We extracted 1396 frequency-dependent phase delays from 273 waveforms on 83 long-period seismograms (62 vertical, 33 radial, and 57 transverse components). These travel times corresponded to about 94% of the data used along the Ryukyu-Hawaii corridor. 64 of the 83 seismograms were recorded on Oahu from 29 Izu-Bonin and 35 Ryukyu events, 17 were recorded on Taiwan from 16 Izu-Bonin and one Hawaiian events, and only 2 of the seismograms were recorded on Japan from two Hawaiian events. We can therefore loosely classify the data into 16 Izu-Bonin-to-Ryukyu paths, 31 Izu-Bonin-to-Hawaii paths, and 36 Ryukyu-to-Hawaii paths; the last one traverse both the Philippine Sea and the Pacific plates while the others traverse only one plate. All the earthquakes were of moderate size ($5.9 < M_W < 7.4$) with well-determined Harvard CMT solutions. Some of the transverse components were also used for *ScS*-reverberations measurements. We also measured 10 multiple *ScS* travel times on the radial components of 4 seismograms recorded at TATO.

The measurement procedure was the same as for the Tonga-Hawaii corridor (Paper I). The recorded seismograms were rotated and low-passed with a zero-phase band-pass filter having corner frequencies at 5 and 45 mHz. Full-mode synthetic seismograms (complete to 50 mHz and filtered like the data) were calculated for each event-station pair using the PA5' reference model (i.e., a model with the velocity structure of PA5 and the Q

structure of Fig. 2c). Isolation filters were constructed for target wavegroups by summing partial sets of normal modes. The measurements were downgraded or eliminated if the agreement was poor either because of low snr or interference by phases not included in the isolation filter (for example, when the *ScS* arrives within the time window of the *SS* arrival). The isolation filters were cross-correlated with the data seismograms, and the resulting time series were windowed and filtered in 5-mHz bands around at discretized set of frequencies between 10 and 45 mHz. The phase delays were determined by fitting Gaussian wavelets to the narrow-band cross-correlagrams and corrected for windowing and filtering effects. Details about the GSDF analyzing procedure can be found in *Gee and Jordan* [1992] and Paper I. Table 1 summarizes the data distribution by wave type.

2.4 Key Features of the Data Set

Some of the key features in the data set are illustrated in Fig. 3, which shows examples of seismograms, isolation filters, and travel-time measurements for a few representative paths. The implications of these observations for mantle structure can be understood by observing a subset of their Fréchet kernels (Fig. 4). These Fréchet kernels were computed by the same 2-D coupled-mode algorithm utilized in Paper I [*Zhao and Jordan*, 1998]. The first example in Fig. 3 focuses on paths that traverse only through the Philippine-Sea plate, from Izu-Bonin to Taiwan. It shows that an *S* wave from a deep-focus event is well modeled by the synthetic isolation filter (top two traces in Fig. 3a), while a Rayleigh wave from a shallow focus event is significantly delayed relative to PA5' (bottom two traces in Fig. 3a). This difference is quantified by the GSDF measurements (Fig. 3b), which show nearly zero travel-time residuals at all frequencies for the *S* wavegroup, but very large phase delays for the R_1 wavegroup, varying from 20 to more than 40 s across the frequency band. In this frequency band, the *S* wave is mostly sensitive to the structure in the transition-zone and in the uppermost mantle near Taiwan, while the R_1 is sensitive to the lid structure and to the uppermost 150 km of the mantle beneath the Philippine Sea. Therefore, the observations directly imply that the uppermost mantle beneath the Philippine Sea is significantly slower than PA5', with the large positive slope of the surface-wave residuals favoring a very slow lid velocity. This interpretation agrees with

the PHB3 model of *Kato and Jordan* [1999] and is confirmed in the inversion discussed in the next section.

The next example demonstrates that paths traversing only the Pacific part of the corridor, from Izu-Bonin to Oahu, produce waveforms that are well fit by the PA5' synthetics (Fig. 3c). For this example, the observed R_1 waveform is advanced by a few seconds, and the S_V and SS_V wavegroups are delayed by 2-5 s (Fig. 3d). The data obtained from paths that traverse from Ryukyu to Hawaii share some of the general features from both the Philippine Sea and the western-Pacific paths. Both the G_1 and the R_1 wavegroups arrive later relative to PA5' (e.g., Fig. 3e), with large dispersion relative to this model (Fig. 3f). These observations confirm that the uppermost mantle beneath the Philippine Sea is significantly slower than beneath the western Pacific. The 2-D Fréchet kernels for some of the measurements are shown in Fig. 4. The diversity of sensitivity, especially in the upper mantle, by various of seismic waves of different frequencies provides excellent resolution to the structure in the upper mantle.

2.5 Inversions for Vertical Tomograms

2.5.1 Parameterization and Inversion Procedure

A data-residual vector of dimension D = 1478 (1396 frequency-dependent phase delays and 82 *ScS* travel times) was inverted for the 2-D structure in the vertical plane of the Ryukyu-Hawaii corridor using the same linear Gaussian-Bayesian inversion scheme that was used for the Tonga-Hawaii corridor (Paper I), with a similar model parameterization. The along-path structure was represented by a perturbation vector $\delta\mathbf{m}$ to the PA5'/PREM reference model $\mathbf{m_0}$ of dimension M=1890, which was organized into three parts:

(1) 1350 blocks representing the relative variations in isotropic shear velocity, $\delta\beta/\beta_0$, over the entire length of the corridor (90°) and depth of the mantle (2879 km). Blocks with a lateral dimension of 1° and an average vertical dimension of 110 km were used in 4 layers above the 410-km discontinuity, 2 in the transition zone, and 5 in the lower mantle from 651 to 1200 km depth (990 blocks in total). Below 1200

km depth, the grid was coarser with 9 layers of 40 blocks each (~2.25° × 250km) extending to the core-mantle boundary. The grid is depicted in Fig. 5a.

(2) 360 blocks representing the relative variations in shear-velocity anisotropy, $(\delta\beta_H - \delta\beta_V)/\beta_0$, in the 4 upper-mantle layers above the 410-km discontinuity.

(3) Two sets of 90 segments each representing the topographic variations, δr_{410} and δr_{660}, for the two major transition-zone discontinuities.

The inversion procedure included two steps. First we inverted the data for a 1-D, path-averaged model, which was employed as the prior model in the second inversion for the final 2-D model. Before the 2-D inversion, a projection was applied to both sides of the linearized perturbation equation to remove the sensitivities of the data to errors in the earthquake origin times and depths (the effect of the latter was considered only for the *ScS* data). Unlike the inversion for the Tonga-Hawaii corridor, an additional crustal correction was applied to the data prior to the inversions by subtracting the *ScS* travel times and the frequency-dependent phase delays predicted from the bathymetry and crustal-thickness variations along the corridor. The bathymetry profile was obtained from the DBDB5 model, whereas the crustal structure was assumed to be those of PA5 (6.8-km thickness), PHB3 (11.5-km thickness) and CRUST5.1 (11.2-km thickness, *Mooney et al.*, 1998) for the Pacific, the Philippine-Sea and the Hawaiian Swell parts of the corridor, respectively. This crustal correction can change the travel-times by up to 10 s for some of the surface-wave data.

The prior covariance matrix was specified using the Gaussian form of Paper I,

$$\overline{C}_{mm}(i,j) = s_{ij}\overline{\sigma}_i\overline{\sigma}_j \exp\left[-(r_i - r_j)^2 / 2l_r^2 - (\theta_i - \theta_j)^2 / 2l_\theta^2\right], \quad (1)$$

where r_i and θ_i are the coordinates at the center of the ith block, and $s_{ij} = s_{ji}$ is a selection coefficient. We adopted the same parameters as in the Tonga-Hawaii study, with horizontal half-width l_θ of 5° and a vertical half width l_r of 250 km, and with the same prior standard deviations, $\{\overline{\sigma}_i\}$, for the individual model parameters (Table 3). Details on the inversion procedure and the prior correlations are given in Paper I.

2.5.2 Model RH2

Prior to the final inversion for the 2-D corridor structure, the entire data set was inverted for a 1-D spherically symmetric perturbation to the reference PA5/PREM model (Fig. 5a). Using this spherically symmetric model as a prior, we inverted for the 2-D model for the Ryukyu-Hawaii corridor, RH2, which is shown in Fig. 5b. This model reveals considerable lateral and vertical variations in the upper mantle, with velocity anomalies as high as +4.6% and as low as -8.9%. Some of the largest velocity anomalies directly reflect the data features discussed in Section 2.4. Qualitatively, the large variation simply expresses the wide distribution of the travel-time residuals measured along the Ryukyu-Hawaii corridor.

In the western part of the corridor, below the Ryukyu and Izu-Bonin subduction zones, the transition zone is dominated by high velocities that mark the two slabs down to the bottom of the transition zone. The slab images in RH2 are consistent with those of *van der Hilst et al.* [1991], *Fukao et al.* [1992] and *van der Hilst et al.* [1997], but they are much wider and smoother in our model because of the longer period and the lower spatial resolution of the seismic data we use here. The fast regions associated with the two subduction zones bound an extremely slow anomaly that covers the uppermost 160 km of the mantle beneath the entire Philippine-Sea section; the lid in this region is 6-8.9% slower than that of PA5, in agreement with the regional 1-D study of *Kato and Jordan* [1999].

In the eastern part of the corridor, near Hawaii, the primary feature is high shear speeds at shallow depths and low shear speeds in the transition zone. Closer to Hawaii this feature overlies a slow region extending from 200 km to the bottom of transition zone, but the upper mantle right beneath the stations at Oahu is faster than PA5, similar to the results for the Tonga-Hawaii corridor and the relatively fast ScS_n-ScS_m residuals observed at KIP from the 1973 Hawaiian event [*Sipkin and Jordan*, 1980]. The exact depth extent of the fast anomaly beneath Hawaii is uncertain, however, because the resolving power of the data set for the vertical structure of this near-receiver region is relatively low. In addition to the isotropic velocity heterogeneity, RH2 also exhibits several small anomalies in radial anisotropy of the uppermost mantle and one larger

negative anomaly reaching -2.2% beneath Hawaii. The latter agrees with the results in Paper I for the Tonga-Hawaii corridor, although the anomaly here is somewhat larger. Unlike in the Tonga-Hawaii model, the topographies on the 410- and 660-km discontinuities are poorly resolved along this corridor, owing to the lack of first-order *ScS*-reverberation times, and they are essentially uncorrelated.

RH2 gives a normalized chi-square $\chi^2/D = 1.26$ (Table 1), which is comparable to that fit obtained in the Tonga-Hawaii inversions (see Table 3 of Paper I). The model yields a total variance reduction of 91%, also similar to the Tonga-Hawaii model, much of which is due to the source statistics and the 1-D structure.

The resolving power of the RH2 inversion has been investigated through a series of checkerboard and other tests (Appendix A). In all resolution tests, a Gaussian noise with standard deviations similar to the error estimates for the real data (up to ~8s) was added to the synthetic data. The upper mantle isotropic velocities are the best resolved parameters in RH2, with horizontal and vertical resolving lengths of about 700 and 200 km or less, respectively. Radial anisotropy in the uppermost mantle and the transition zone topographies are less resolved. The checkerboard tests indicate that isotropic velocity variations are not appreciably mapped into radial anisotropic heterogeneity or into topographic variations on the 410- and 660-km discontinuities.

Chapter 3

Seismic Structure of the Mantle Along the Mariana, Solomon, and Noumea-Hawaii Corridors

Using the same technique described by Paper I and in the previous chapter, we inverted the data from individual source arrays in Mariana, Solomon, and New Hebrides Island for 2-D vertical tomograms of mantle structure, which are shown in Fig. 7. The 2-D tomograms for these corridors are generally consistent with previous tomographic results, although they show upper-mantle features that are smaller in scale and larger amplitude than published global models.

3.1 Model MH1

Model MH1 was inverted using a data set with 1486 frequency-dependent phase delays and 28 *ScS* travel times for the vertical plane of the Mariana-Hawaii corridor. It shows that there is a slow anomaly in the transition zone beneath the Hawaiian Swell and the western edge of the old part of Pacific plate just right before they subducted into Mariana trench. Most of the Pacific plate between Mariana and Hawaii shows a fast anomaly in the upper mantle and slow anomaly in the transition zone.

3.2 Model SH1

Using a data set with 1649 frequency-dependent phase delays and 42 *ScS* travel times, model SH1 which was inverted for the 2-D structure in the vertical plane of the Solomon-Hawaii corridor has similar features compared with model MH1 except that it has a little larger amplitude than other corridors. There is an obvious fast anomaly in the upper mantle beneath Solomon Island. There is also a slow anomaly in the transition zone

beneath the western edge of the Pacific plate and Hawaiian Swell. The slow velocity extends from 400 km to 1500 km beneath the Pacific plate.

3.3 Model NH1

Model NH1 was inverted with a data set of 1704 frequency-dependent phase delays and 38 *ScS* travel times for the 2-D structure in the vertical plane of the Noumea-Hawaii corridor. It shows some different features. The slow velocity anomaly appears in the upper mantle west of the Hawaii area. There is a fast anomaly in the transition zone beneath the Hawaiian Swell. The uppermost mantle of the western part of Pacific plate between Noumea and Hawaii is fast, as is the transition zone beneath Noumea.

Some care should be paid on the resolving power of different corridors. Resolution tests confirmed the ability of the data set to resolve upper-mantle shear-velocity structures along individual corridors with scale lengths less than 700 km horizontally and 200 km vertically, although their resolving power diminish rapidly below the 660 km discontinuity. The resolution tests also show that the resolving power for model NH1 is worse than other corridors because of the relatively sparse source distribution.

Chapter 4

3-D Seismic Structure of the Mantle Beneath the Southwestern Pacific (SWP1)

To improve the tomographic resolution of upper-mantle structure beneath the western Pacific basin, we have collected extensive sets of frequency-dependent travel times from circum-Pacific earthquakes recorded by broadband seismometers in this region. A variety of seismic phases were analyzed in the band 10-50 mHz, including direct and multiple S waves, Love and Rayleigh surface waves, and ScS reverberations. In our initial experiments, we inverted the data from individual source arrays in the New Hebrides, Solomon, Mariana, Izu Bonin-Ryukyu, and Japan Island arcs for 2-D vertical tomograms of mantle structure using the technique described in Paper I and chapter 2.

A natural extension to the inversion approach is the incorporation of multiple-crossing paths into a full 3-D inversion. A data-residual vector of dimension D = 7899 (7563 frequency-dependent phase delays and 336 ScS travel times) was inverted for the 3-D structure beneath the southwestern Pacific using the same linear Gaussian-Bayesian inversion scheme that was used for the 2-D inversions (Table 2). The 3-D structure was represented by a perturbation vector $\delta\mathbf{m}$ to the PA5/PREM reference model $\mathbf{m_0}$ of dimension M = 7431. It was organized into three parts:

(1) 4297 blocks representing the relative variations in isotropic shear velocity, $\delta\beta/\beta_0$, over the entire length of five corridors and depth of the mantle (2879 km). Blocks with a lateral dimension of 1.2° and an average vertical dimension of 150 km were used in 4 layers above the 410-km discontinuity, 2 in the transition zone, and 3 in the lower mantle from 651 to 1200 km depth. Below 1200 km depth, the grid was coarser with 7 layers (~2.5° × 300km) extending to the core-mantle boundary.

(2) 1495 blocks representing the relative variations in shear-velocity anisotropy, $(\delta\beta_H - \delta\beta_V)/\beta_0$, in the 4 upper-mantle layers above the 410-km discontinuity.

(3) 1639 blocks representing the topographic variations, δr_{410} and δr_{660}, for the two major transition-zone discontinuities.

The solution to the Bayesian inverse problem is

$$\boldsymbol{\delta m} = \overline{\boldsymbol{\delta m}} + (\boldsymbol{A}^T \cdot \boldsymbol{A} + \overline{\boldsymbol{C}}_{mm}^{-1})^{-1} \cdot \boldsymbol{A}^T \cdot (\boldsymbol{\delta d} - \boldsymbol{A} \cdot \boldsymbol{\delta m}), \tag{2}$$

with the prior covariance matrix (in Gaussian form):

$$\overline{C}_{mm}(i,j) = s_{ij}\overline{\sigma}_i\overline{\sigma}_j \exp\left[-(r_i - r_j)^2 / 2l_r^2 - (\theta_i - \theta_j)^2 / 2l_\theta^2 - (\varphi_i - \varphi_j)^2 / 2l_\varphi^2\right], \tag{3}$$

where $\boldsymbol{A}$ is the partial derivative matrix, $\delta\boldsymbol{d}$ is the data residual vector, r_i, θ_i, and φ_i are the coordinates at the center of the ith block, and $s_{ij} = s_{ji}$ is a selection coefficient. We adopted the same parameters as in the Tonga-Hawaii study, with horizontal half-width l_θ and l_φ of 5° and a vertical half width l_r of 250 km, and with the same prior standard deviations, $\{\overline{\sigma}_i\}$, for the individual model parameters (Table 3).

We then inverted the entire data set from all corridors for a 3-D model of the southwestern Pacific upper mantle (Fig. 8). At low wavenumbers, this regional model is consistent with large-scale features found from global tomography. For example, the uppermost mantle (< 200 km depth) shows fast anomalies in the interior of the Pacific plate and slow anomalies in the marginal basins along the Pacific Rim, while this pattern is reversed in the transition zone (400-700 km). However, our model displays greater lateral heterogeneity in both isotropic and anisotropic structure than the global models, especially in the 200-400 km depth range, which can be attributed to the better resolution of small-scale features by our data set. Fast and slow anomalies in isotropic shear speed, some extended subparallel to the Pacific plate motion, are observed in the upper mantle. In particular, the Hawaiian Swell is underlain by a fast anomaly in the uppermost mantle and a slow anomaly in the transition zone. Near Hawaii, the amount of radial anisotropy is smaller than its surrounding regions, which is inconsistent with a recent study of global anisotropy by *Ekström and Dziewonski* (1998) (Fig. 9). Our tomographic results for the southwestern Pacific indicate that the upper mantle in this region is chemically heterogeneous and dynamically active.

Chapter 5

Discussion

The Ryukyu-Hawaii corridor extends several thousands of kilometers west of the Hawaiian Swell, where it samples an old part of the Pacific plate. Comparing our results with previous global studies (*Su et al.,* 1994; *Masters et al.,* 1996; *Ekström and Dziewonski*, 1998), we found generally good agreement in large-scale features (Fig. 6). All models show a low-velocity anomaly in the transition zone beneath the Pacific plate, and a high-velocity anomaly in the lower-most mantle. Due to the differences in resolving power and data sets, the global models also show some disagreements, e.g., the different amplitudes, different velocity anomalies beneath the Hawaiian Swell and Philippine Sea, etc. Our model lies within the variance of the global models. Furthermore, our result contains finer details of the velocity variation with better lateral and horizontal resolving power. The two most dominant features in the upper mantle are: (1) Low shear-wave speeds at shallow depths and high speeds in the transition zone beneath the Philippine Sea; (2) High shear speeds at shallow depths and low speeds in the transition zone beneath the Pacific part of the corridor.

The shear velocity in the uppermost 160 km of the mantle beneath the Philippine Sea is 3.5% to 8.9% slower than the reference model PA5, and the average lid velocity in this region is 6.9% slower (Fig. 5b). These variations are too large to be explained by the difference in plate age [*Nishimura and Forsyth*, 1989].

The same large variation, 5.8%, is observed between the lid velocities of PA5 (4.75 km/s) and PHB3 (4.48 km/s). *Kato and Jordan* [1999] and *Gaherty et al.* [1999] argued that this contrast couldn't be due to temperature alone because the lid appears to be thinner in the old, central Pacific and thicker in the younger Philippine Sea. Instead, they proposed that the G discontinuity, which marks the bottom of the lid, represents the depth of melting in the ridge environment; they further speculated that this depth is larger in the Philippine Sea due to the presence of extra water [*Hirth and Kohlstedt*, 1996], provided

by the long history of subduction around the area, which decreases its melting temperature and its seismic velocity [*Sato et al.*, 1989; *Karato*, 1995]. Compositional variation of this kind can also explain the large velocity heterogeneity observed by *Lebedev et al.* [1997] across the Central Basin Ridge, which is hard to reconcile with thermal variation alone.

The Pacific part of the corridor has high average shear speeds in the shallow mantle, which are required by the negative phase delays observed for surface waves propagating between Izu-Bonin and Hawaii (Fig. 3d). However, the multiple *S*-wave phase delays are generally positive, yielding lower speeds in the sub-lithospheric mantle below about 250km depth along the eastern half of the corridor. The lowest shear speeds are within distinct upper-mantle anomaly at a depth of 200-400km beneath the Hawaiian Swell. The average shear speeds of the swell above 200km are lower than those found to the west, but they are still greater than the PA5 reference model. These high shear velocities indicate that the Hawaiian Swell is likely not supported by thermal bouyancy at shallow depths. The problem of associating the Hawaiian Swell with a strictly thermal origin, such as lithospheric rejuvenation [*Detrick and Crough*, 1978; *Crough*, 1983], has already been raised by others. Two-station measurements of Rayleigh-wave dispersion between Midway and Oahu found no evidence for lithospheric thinning between Midway and Oahu [*Woods and Okal*, 1996]. Heat flow measurements taken along a profile transverse to the swell also found no anomaly that correlates with the swell location [*Von Herzen et al.*, 1989]. As discussed in Paper I, a plausible way to generate a high-velocity, buoyant mantle is by a basaltic-differentiation mechanism, which depletes the source region from its incompatible elements (Fe, Al) and strips it from its volatiles (H_2O, CO_2). Depletion of Fe and Al causes a significant reduction in the density [*O'Hara*, 1975; *Green and Liberman*, 1976; *Oxburgh and Parmentier*, 1977; *Jordan*, 1979] as well as a slight increase in the seismic velocity [*Jordan*, 1979], whereas the extraction of volatiles elevates the solidus temperature [*Hirth and Kohlstedt*, 1996], which leads to a significant increase in the seismic velocity [*Sato et al.*, 1989; *Karato*, 1995], especially if the homologous temperature is higher than 0.95. This chemical-differentiation mechanism was invoked by *Sipkin and Jordan* [1980] to explain their multiple-*ScS* data beneath Hawaii, and its dynamical implications were investigated by *Phipps Morgan et al.* [1995].

The latter study showed that the amount of basalt depletion that is expected from the extra crustal area across the Hawaiian chain could account for most of the swell relief.

We have also obtained the perturbation in radial anisotropy above the 410-km discontinuity, although it is less resolved than the isotropic part. Fig. 5b shows the anisotropic perturbation with respect to their values in the reference model PA5. The amount of radial anisotropy, quantified by $(\delta\beta_H - \delta\beta_V)/\beta_0$, is minimum near Oahu, which is consistent with the result in Paper I obtained from the almost perpendicularly oriented Tonga-Hawaii path. It is possible to reconcile this observation with a strong, coherent azimuthal anisotropy. The projections of azimuthal anisotropy onto the two nearly perpendicular paths are more likely to yield different radial-anisotropy ratios [*Maupin*, 1985], and it is plausible that the amount of radial anisotropy is, indeed, smaller near Hawaii. Such an anomaly can also originate from lattice-preferred orientation of olivine due to vertical flows beneath Oahu, or from a large disturbance in the previously predominantly horizontal alignment due to a vigorous convection near the hotspot. However, this feature in both TH2 for Tonga-Hawaii corridor and RH2 appears to be in disagreement with the recently published result by *Ekström and Dziewonski* [1998] who concluded that the radial anisotropy at the depth around 150km beneath the Pacific plate are the strongest near Hawaii.

Chapter 6

Conclusions

We have presented a high-resolution, composite model, RH2, for the 2-D mantle structure in the plane of the Ryukyu-Hawaii corridor. We found that high shear speed at shallow depths and low speed in the transition zone under the Pacific part of the corridor; very low shear speed within a distinct upper-mantle anomaly at the depths of 200-400km near the Hawaiian Swell. The northern Philippine Sea is underlain by very slow seismic velocities in the uppermost mantle and high velocities in the transition zone above the 660-km discontinuity. The high shear speed at shallow depths and low speed in the transition zone beneath the Pacific part of the corridor are largely unbiased by lateral heterogeneity perpendicular to the path, and robust with respect to uncertainties in radial anisotropy and transition-zone discontinuity topographies. The high shear velocity in the uppermost mantle near Oahu indicates that the Hawaiian Swell is not supported by higher temperatures at shallow depths, as predicted, for example, by the thermal rejuvenation model of *Detrick and Crough* [1978]. Instead, thermal buoyancy associated with the deeper low-velocity anomaly in the transition zone may play a role, although we should point out that this anomaly is centered on a local minimum in the swell topography.

A natural extension to the inversion approach employed here and in Paper I is the incorporation of multiple-crossing paths into a full 3-D inversion. In our 3-D regional model, we found the familiar large-scale features found from global tomography. For example, the uppermost mantle (< 200 km depth) shows fast anomalies in the interior of the Pacific plate and slow anomalies in the marginal basins along the Pacific rim, while this pattern is reversed in the transition zone (400-700 km). However, our model displays greater lateral heterogeneity in both isotropic and anisotropic structure than the global models, especially in the 200-400 km depth range, which can be attributed to the better resolution of small-scale features by our data set. Fast and slow anomalies in isotropic shear speed, some extended subparallel to the Pacific plate motion, are observed in the

upper mantle. In particular, the Hawaiian Swell is underlain by a fast anomaly in the uppermost mantle and a slow anomaly in the transition zone. Near Hawaii, the amount of radial anisotropy is smaller than its surrounding regions, which is inconsistent with a recent study of global anisotropy by *Ekström and Dziewonski* (1998). Our tomographic results for the southwestern Pacific indicate that the upper mantle in this region is chemically heterogeneous and dynamically active.

Appendix A

Resolution Tests

We investigated the resolving power of our 2-D GSDF method and the data set by inverting synthetic data sets computed for a series of input models. In all these tests, a Gaussian noise with standard deviations similar to our error estimates for the real data (up to ~8 s) was added to the synthetic data prior to the inversions.

We first inverted a synthetic data set with only the Gaussian noise to examine the effect of random errors. The maximum perturbations in the resulting model shown in Fig. A1 (a) are 4 times smaller than those in RH2 for both velocity (isotropic and anisotropic) and topography parameters. The rms heterogeneity in Fig. A1 (a) is also significantly smaller than in RH2 (by more than a factor of 4 for the isotropic and topographic parameters, and by about a factor of 3 for the anisotropic parameters), demonstrating that the model is not significantly biased by random errors in the data. This was particularly true for the large isotropic variation in the uppermost 160 km of the mantle (where the rms ratio exceeds 6.5).

The remaining examples in Fig. A1 demonstrate the recovery capability for the structural features within the mantle corridor. In the first test (Fig. A1 (b)), we inverted the residuals predicted by RH2 (after adding the Gaussian noise), and obtained a model which nicely reproduced all the upper-mantle features of the input model with the right amplitude and with almost no smearing. The recovery of the transition-zone structure was also good, although the structural smearing was more pronounced, especially below the Philippine Sea. The other features in the model were relatively poorly recovered and their magnitudes underestimated the original, particularly for some of the lower-mantle anomalies. The topographies were the least robust parameters in RH2, as discussed below.

Despite the greater length of the Ryukyu-Hawaii corridor, the resolution of the upper-mantle structure was comparable to that achieved along the Tonga-Hawaii corridor in

Paper I, owing to the larger data set and the multiple stations employed here. Checkerboard tests indicate that perturbations with a scale length of about 700km are well resolved both horizontally and vertically in the upper mantle (Fig. A1 (c-f)). The resolution, however, degraded substantially in the lower mantle, which was only sparsely sampled by the *S* and *ScS* waves. Below the 660-km discontinuity, small features could no longer be resolved, and perturbations with a scale length of 2000km or more were smeared along the wave paths (Fig. A1 (d)). Hence, the positive mid-mantle anomaly in RH2 could result from this wave-path smearing effect. It is noteworthy that, despite the poor lateral resolution in the lower mantle, path-average properties can still be well recovered. The inversion experiments shown in Fig. A1 indicate that isotropic velocity variations are not appreciably mapped into radial anisotropic heterogeneity or into topographic variations. Other inversion experiments not shown here indicate that the reverse also holds: topography and anisotropy do not map into isotropic velocities. We conclude, therefore, that in addition to the good upper-mantle resolution in RH2, the trade-offs between parameters of different types in this model are insignificant.

Acknowledgments. I thank Li Zhao, R. D. van der Hilst, and J. McGuire for insightful discussions; the IRIS-DMC for the digital seismic records; and Harvard Seismology Group for their CMT solutions. Some of the figures were generated using the GMT software freely distributed by *Wessel and Smith* [1991]. This research was supported by the National Science Foundation under grant EAR-9628351.

Bibliography

Butler, R., The 1973 Hawaii earthquake: a double earthquake beneath the volcano Mauna Kea, *Geophys. J. R. astr. Soc.*, *69*, 173–186, 1982.

Crough, S. T., Hotspot swells, *Ann. Rev. Earth Planet. Sci*, *11*, 165–193, 1983.

Detrick, R. S., and S. T. Crough, Island subsidence, hot spots, and lithospheric thinning, *J. Geophys. Res.*, *83*, 1236–1244, 1978.

Dziewonski, A. M., and D. L. Anderson, Preliminary reference earth model, *Phys. Earth Plant. Int.*, *25*, 297-356, 1981.

Dziewonski, A. M., G. A. Ekström, and X.-F. Liu, Structure at the top and bottom of the mantle, in *Monitoring a Comprehensive Test Ban Treaty*, edited by E. S. Husebye, and A. M. Dainty, pp. 521–550, Kluwer Academic Publishers, Dordrecht, 1996.

Ekström, G. A., and A. M. Dziewonski, The unique anisotropy of the Pacific upper mantle, *Nature, 394,* 168-172, 1998.

Forte, A. M., A. M. Dziewonski, and R. L. Woodward, Aspherical structure of the mantle, tectonic plate motions, nonhydrostatic geoid, and topography of the core-mantle boundary, in *Dynamics of Earth's deep interior and Earth rotation, Geophys. Monogr. Ser*, edited by J.-L. Le Mouel, D. E. Smylie, and T. Herring, *72*, pp. 135–166, 1993.

Fukao, Y., M. Obayashi, H. Inoue, and M. Nenbai, Subducting slabs stagnant in the mantle transition zone, *J. Geophys. Res.*, *97*, 4809–4822, 1992.

Gaherty, J. B., T. H. Jordan, and L. S. Gee, Seismic structure of the upper mantle in a western Pacific Corridor, *J. Geophys. Res.*, *101*, 22,291–22,309, 1996.

Gaherty, J. B., M. Kato, and T. H. Jordan, Seismological structure of the upper mantle: A regional comparison of seismic layering, *Phys. Earth Planet. Inter., 110,* 21-41, 1999.

Gee, L. S., and T. H. Jordan, Generalized seismological data functionals, *Geophys. J. Int.*, *111*, 363-390, 1992.

Green, D. H., and R. C. Liberman, Phase equilibria and elastic properties of a pyrolite model for the oceanic upper mantle, *Tectonophysics*, *32*, 61–92, 1976.

Gripp, A. E., and R. G. Gordon, Current plate velocities relative to the hotspots incorporating the NUVEL-1 global plate motion model, *Geophys. Res. Lett.*, *17*, 1109–1112, 1990.

Hager, B. H., and R. W. Clayton, Constraints on the structure of mantle convection using seismic observations, flow models, and the geoid, in *Mantle Convection: Plate Tectonics and Global dynamics*, edited by W. R. Peltier, pp. 658–763, Gordon And Bench, New York, 1989.

Hirth, G., and D. L. Kohlstedt, Water in the oceanic upper mantle: implications for the rheology, melt extraction and the evolution of the lithosphere, *Earth Planet. Sci. Lett.*, *144*, 93–108, 1996.

Jordan, T. H., Mineralogies, densities and seismic velocities of garnet lherzolites and their geophysical implications, in *Mantle Sample: Inclusions in Kimberlites and other volcanics*, edited by F. R. Boyd, and H. O. A. Meyer, pp. 1-13, American Geophysical Union, Washington, D.C., 1979.

Karato, S.-I., Effects of water on seismic wave velocities in the upper mantle, *Proc. Japan. Acad.*, *71*, 61–66, 1995.

Karato, S.-I., S. Zhang, and H.-R. Wenk, Superplasticity in Earth's lower mantle: evidence from seismic anisotropy and rock physics, *Science*, *270*, 458–461, 1995.

Kato, M., and T. H. Jordan, Seismic structure of the upper mantle beneath the western Philippine Sea, *Phys. Earth Planet. Inter.*, *110*, 263-283, 1999.

Katzman, R., L. Zhao, and T. H. Jordan, High-resolution, 2D vertical tomography of the central Pacific mantle using *ScS* reverberations and frequency-dependent travel times, *J. Geophys. Res.*, *103*, 17,933-17,971, 1998.

Lebedev, S., G. Nolet, and R. v. d. Hilst, The upper mantle beneath the Philippine Sea region from waveform inversion, *Geophys. Res. Lett.*, *24*, 1851–1854, 1997.

Li, X.-D., and B. Romanowicz, Global mantle shear velocity model developed using nonlinear asymptotic coupling theory, *J. Geophys. Res.*, *101*, 22,245–22,272, 1996.

Masters, G., S. Johnson, G. Laske, and H. Bolton, A shear velocity model of the mantle, *Philos. Trans. R. Soc. London, Ser. A*, *354*, 1385-1411, 1996.

Maupin, V., Partial derivatives of surface-wave phase velocities for flat anisotropic models, *Geophys. J. R. Astron. Soc.*, *83*, 379–398, 1985.

McKenzie, D., and M. J. Bickle, The volume and composition of melt generated by extension of lithosphere, *J. Petrol.*, *29*, 625–679, 1988.

Montagner, J.-P., and B. L. N. Kennett, How to reconcile body-wave and normal mode reference Earth models, *Geophys. J. Int.*, *125*, 229–248, 1996.

Mooney, W. D., laske, G. and Masters, G., CRUST5.1: A global crustal model at 5°× 5°, *J. Geophys. Res., 103*, 727-747, 1998.

Mueller, R. D., W. R. Roest, J.-Y. Royer, L. M. gahagan, and J. G. Sclater, A digital age map of the ocean floor, *SIO reference series 93-30*, 1993.

Nishimura, C. E., and D. W. Forsyth, The anisotropic structure of the upper mantle in the Pacific, *Geophys. J. Int.*, *96*, 203, 1989.

O'Hara, M. J., Is there an Icelandic mantle plume?, *Nature*, *253*, 708–710, 1975.

Oxburgh, E. R., and E. M. Parmentier, Compositional and density stratification in oceanic lithosphere—causes and consequences, *J. Geol. Soc. Lond.*, *133*, 343–355, 1977.

Phipps Morgan, J., and P. Shearer, Seismic constraints on mantle flow and topography of the 660-km discontinuity: Evidence for whole mantle convection, *Nature*, *365*, 1993.

Phipps Morgan, J., W. J. Morgan, and E. Price, Hotspots melting generates both hotspot volcanism and hotspot swell, *J. Geophys. Res.*, *100*, 8045–8062, 1995.

Puster, P., and T. H. Jordan, How stratified is mantle convection?, *J. Geophys. Res.*, *102*, 7625–7646, 1997.

Regan, J., and D. L. Anderson, Anisotropy models of the upper mantle, *Phys. Earth Plant. Inter.*, *35*, 227–263, 1984.

Richter, F., and B. Parsons, On the interaction of two scales of convection in the mantle, *J. Geophys. Res.*, *80*, 2529–2541, 1975.

Romanowicz, B., A global tomographic model of shear attenuation in the upper mantle, *J. Geophys. Res.*, *100*, 12,375–12,394, 1995.

Sato, H., I. S. Sacks, and T. Murase, The use of laboratory velocity for estimating temperature and partial melt fraction in the low-velocity zone: comparison with heat flow and electrical conductivity studies, *J. Geophys. Res.*, *94*, 5689–5704, 1989.

Sipkin, S. A., and T. H. Jordan, Regional variation of QScS, *Bull. Seismol. Soc. Am.*, *70*, 1071–1102, 1980.

Su, W.-J., R. L. Woodward, and A. M. Dziewonski, Degree 12 model of shear velocity heterogeneity in the mantle, *J. Geophys. Res.*, *99*, 6945–6980, 1994.

Van der Hilst, R., R. Engdahl, W. Spakman, and G. Nolet, Tomographic imaging of subducted lithosphere below northwest Pacific island arcs, *Nature*, *353*, 37-43, 1991.

Van der Hilst, R., S. Widiyantoro, and E. R. Engdahl, Evidence for deep mantle circulation from global tomography, *Nature*, *386*, 578–584, 1997.

Von Herzen, R. P., M. J. Cordery, R. S. Detrick, and C. Fang, Heat flow and thermal origin of hotspot swells: The Hawaiian Swell revisited, *J. Geophys. Res.*, *94*, 13,783–13,799, 1989.

Wessel, P., Observational constraints on model of the Hawaiian hot spots swell, *J. Geophys. Res.*, *98*, 16,095–16,104, 1993.

Woodhouse, J. H., and A. M. Dziewonski, Mapping the upper mantle: Three dimensional modeling of earth structure by inversion of seismic waves, *J. Geophys. Res.*, *89*, 5953–5986, 1984.

Woods, M. T., and E. A. Okal, Rayleigh-wave dispersion along the Hawaiian Swell: a test of lithospheric thinning by thermal rejuvenation, *Geophys. J. Int.*, *125*, 325–339, 1996.

Zhang, Y.-S., and T. Tanimoto, Three-dimensional modeling of upper mantle structure under the Pacific ocean and surrounding area, *Geophys. Res. J. R. Astron. Soc.*, *98*, 255–269, 1989.

Zhang, Y.-S., and T. Tanimoto, Global Love wave phase velocity variation and its significance to plate tectonics, *Phys. Earth. Plant. Inter.*, *66*, 160–202, 1991.

Zhang, Y.-S., and T. Tanimoto, High-resolution global upper mantle structure and plate tectonics, *J. Geophys. Res.*, *98*, 9793-9823, 1993.

Zhao, L., and T. H. Jordan, Sensitivity of frequency-dependent travel times to laterally heterogeneous, anisotropic Earth structure., *Geophys. J. Int., 133*, 683-704, 1998.

Zhou, H.-W., and R. W. Clayton, *P* and *S* wave travel time inversions for subduction slab under the island arcs of the northwest pacific, *J. Geophys. Res.*, *95*, 6829–6851, 1990.

Table 1. Summary of the inversion results for 2-D model RH2

Phase	Number of Data	Data Importance	χ^2/D Reference Model	χ^2/D After Denuis.*	χ^2/D After Inversion	Variance Reduction
Rayleigh	232	4.36	46.50	17.62	2.79	0.94
Love	171	4.69	5.61	2.74	1.51	0.73
S_V	281	7.62	14.45	3.44	0.92	0.94
S_H	222	4.19	7.08	1.76	0.70	0.90
SS_V	134	5.20	3.53	1.70	0.60	0.83
SS_H	97	4.43	11.10	1.41	0.52	0.95
SSS_V	137	7.74	1.95	2.34	1.06	0.45
SSS_H	96	6.53	13.17	2.28	1.59	0.88
Other guided waves	16	0.31	1.02	2.02	2.13	-1.09
ScS on R component (GSDF)	10	0.40	1.05	1.63	0.42	0.60
ScS on T component (ray)	82	6.40	14.51	6.27	0.84	0.94
All phases	1478	51.86	14.67	5.00	1.26	0.91

Table 2. Summary of the inversion results for 3-D model SWP1

Phase	Number of Data	Data Importance	χ^2/D Reference Model	χ^2/D After Denuis.*	χ^2/D After Inversion	Variance Reduction
Rayleigh	1456	17.5	45.38	13.3	2.79	0.94
Love	967	22.73	36.88	8.22	2.11	0.94
S_V	1621	27.92	14.54	3.09	1.46	0.9
S_H	1359	17.54	7.54	4.67	1.27	0.83
SS_V	1108	23.45	7.18	2.11	0.82	0.89
SS_H	191	8.96	9.39	1.86	1.02	0.87
SSS_V	496	17.41	7.34	3.7	1.42	0.81
SSS_H	181	6.91	15.08	3.8	1.7	0.89
Other guided waves	16	0.44	5.74	5.98	3.3	0.42
ScS on R component (GSDF)	158	8.22	163.35	9.84	3.67	0.98
ScS on T component (ray)	336	22.93	125.01	9.15	1.48	0.99
All phases	7899	174.87	27.8	6.16	1.73	0.94

* This column shows the χ^2 estimates (normalized by the number of data) after projecting the errors in source origin-time (and source depth for the *ScS* reverberation measurements) out of the original data.

Table 3. Summary of the inversion parameters

model	$\bar{\sigma}_{UM}$ (%)	$\bar{\sigma}_{TZ}$ (%)	$\bar{\sigma}_{LM}$ (%)	$\bar{\sigma}_{AN}$ (%)	$\bar{\sigma}_{410}$ (km)	$\bar{\sigma}_{660}$ (km)	$\frac{\chi^2_{GSDF}}{D}$	$\frac{\chi^2_{ScS}}{D}$	$\frac{\chi^2_{TOT}}{D}$
RH2	2.5	1	0.5	0.8	10	10	1.28	0.84	1.26
SWP1	2.0	1	0.5	0.5	10	10		1.48	1.73

* The standard deviations, $\{\bar{\sigma}_i\}$, are explained in Paper I.

Figure captions

Figure 1. Mercator projection of the studied area in the southwestern Pacific. Dashed lines mark the paths sampled by the Ryukyu-Hawaii corridor of this study and by the Mariana, Solomon, Noumea, and Tonga-Hawaii corridors for 3-D inversion. Inverse black triangles show the stations and white symbols show the epicenters of the events used in this study (circles: shallow-focus; diamonds: intermediate-focus; squares: deep-focus). Black arrows are the current plate motion relative to the hotspot reference frame [*Gripp and Gordon*, 1990].

Figure 2. (a) Comparison of the mean shear-wave speeds between two models, PA5 model [*Gaherty et al.*, 1996] and PREM [*Dziewonski and Anderson*, 1981]. and are the two shear-wave speeds in a radially anisotropic model. The velocity structures of PA5 for the upper mantle and PREM for the lower mantle are chosen as the reference model. (b) Shear Q structure of PA5, used in Paper I for the Tonga-Hawaii corridor. (c) Shear Q structure of PA5', used in this study for the Ryukyu-Hawaii corridor. In both models, the Q value for the entire lower mantle is 231. (d) Examples of seismograms recorded at HON from shallow Izu-Bonin event. Top triplet is vertical-component; bottom triplet is transverse component. In each triplet, top trace is data, middle trace is synthetic calculated using the PA5/PREM model, and bottom trace is synthetics calculated using the PA5'/PREM model (i.e., the velocity structure of PA5/PREM and the Q structure of Figure 2c). The latter model, which matches the surface-wave amplitudes better, was used to calculate the synthetic seismograms in the data processing.

Figure 3. The GSDF process. The panels on the left are recorded seismograms and isolation filters for the target seismic phases computed for PA5'/PREM, plotted separately for the Philippine Sea part, the Pacific part, and the entire length of the studied corridor. The panels on the right are the frequency-dependent phase delays for R_1 (red triangle), G_1 (cyan triangle), S_V (blue circle), S_H (green circle), and SS_V (magenta square) waves.

Figure 4. Examples of 2-D Fréchet kernels for the mean shear-wave speed computed by coupled-mode summation. The wave type and frequency are indicated at the top of each panel. Warm colors correspond to negative sensitivity (phase-delay increase for velocity

decrease), cool colors to positive sensitivity, and the green solid lines show the sensitivities to perturbations in the depths of the 410- and 660-km discontinuities; yellow circle and blue triangle show the locations of the source and receiver, respectively.

Figure 5. (a) The 1-D path average model obtained from inverting the Ryukyu-Hawaii data set, shown in a cross-section through the mantle from Ryukyu (left side) to Hawaii (right side). The grid displayed here was used for all the inversions. This model was taken as the prior for the 2-D inversions. (b) RH2, the preferred 2-D model. The model is displayed as shear-velocity perturbations relative to PA5/PREM. Lower plot in each panel shows the relative perturbation in isotropic shear velocity extending from the Moho discontinuity (M) to the core-mantle boundary (CMB); negative perturbations are in red, positive in blue. Upper plot in each panel uses the same color scale to show the relative perturbation in radial anisotropy, and green and red lines to represent the perturbations to the 410- and 660-km discontinuities, respectively (5× vertical exaggeration). Yellow circles are earthquakes used as sources; blue triangle marks locations of the stations.

Figure 6. Comparison of the model RH2 (relative to PA5/PREM) with the global 3-D models (relative to PREM) and S20A [*Ekström and Dziewonski,* 1998], S16B30 [*Masters et al.,* 1996], and SKS12WM13 [*Su et al.,* 1994] along the same corridor.

Figure 7. 2-D models for five corridors beneath the southwestern Pacific, RH2 for Ryukyu-Hawaii corridor, MH1 for Mariana-Hawaii corridor, SH1 for Solomon-Hawaii corridor, NH1 for Noumea-Hawaii corridor, and TH2 for Tonga-Hawaii corridor. The same conventions as in Fig. 5 have been used.

Figure 8. Comparison of the 3-D regional model SWP1 of this study with the global model S20A for the isotropic shear-wave velocity variations at depth of 100, 300, and 500km.

Figure 9. Comparison of the 3-D regional model SWP1 of this study with the global model S20A for the anisotropic shear-wave velocity variations at depth of 50, 100, and 150km.

Figure A1. Examples of resolution tests, with models displayed as in Fig. 6b. In all the examples, synthetic data were generated by adding the same realistic Gaussian noise to

phase delays computed from the input models and inverting them with the same procedure as for RH2. (a) Output model obtained by inverting Gaussian noise only. (b) Output model from an inversion of the data residuals predicted by RH2 (Fig. 6b). (c) Input model with harmonic variation in shear velocities, having a horizontal and vertical wavelengths of 40° and 4000 km. (d) The recovered model for the structure in (c). (e) Input model with horizontal and vertical wavelengths of 15° and 1500 km. (f) The recovered model for the structure in (e).

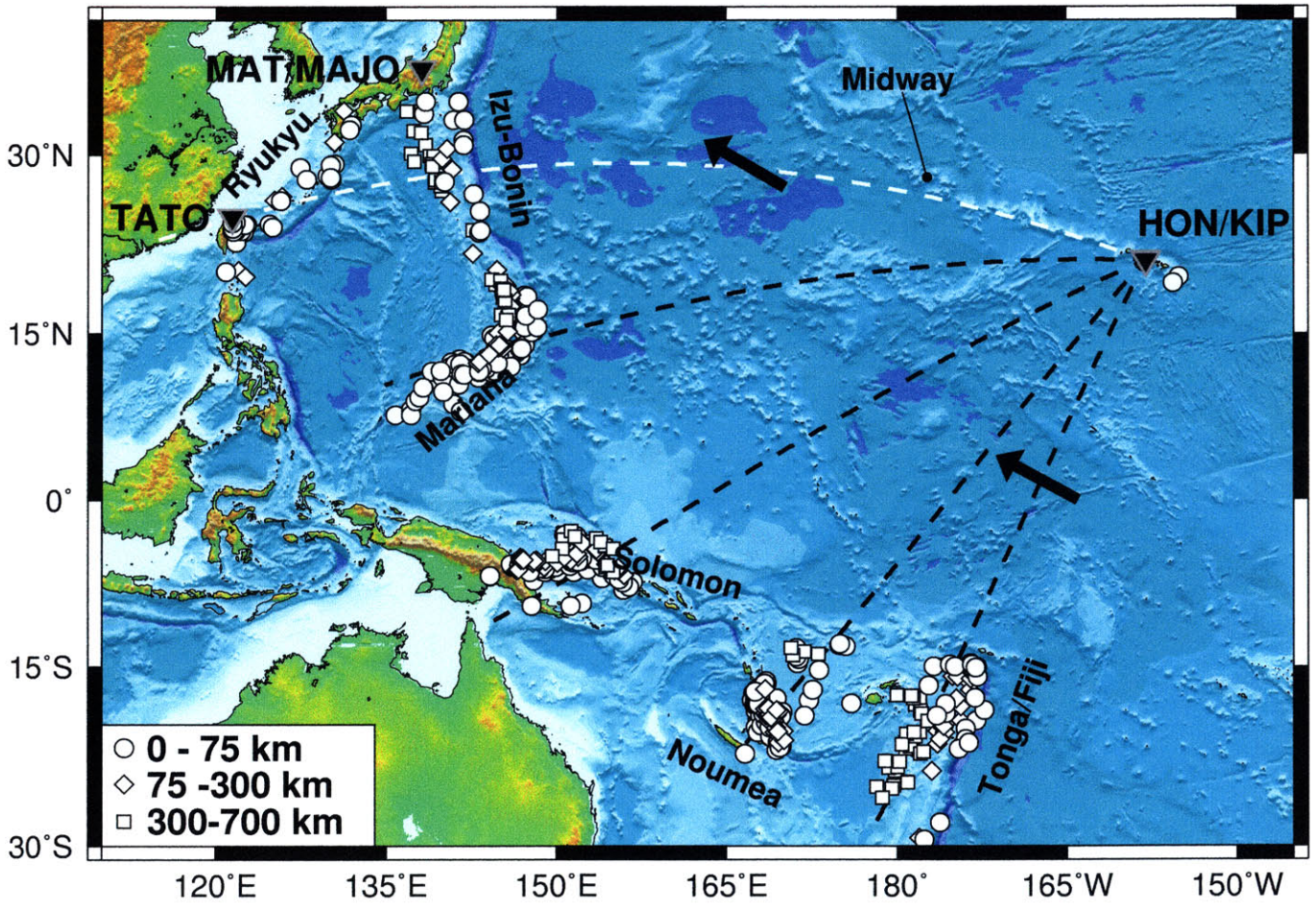
MAT/MAJO
Midway
Izu-Bonin
Ryukyu
TATO
HON/KIP
30°N
15°N
0°
15°S
30°S
Mariana
Solomon
Noumea
Tonga/Fiji
0 - 75 km
75 -300 km
300-700 km
120°E
135°E
150°E
165°E
180°
165°W
150°W

Fig. 1

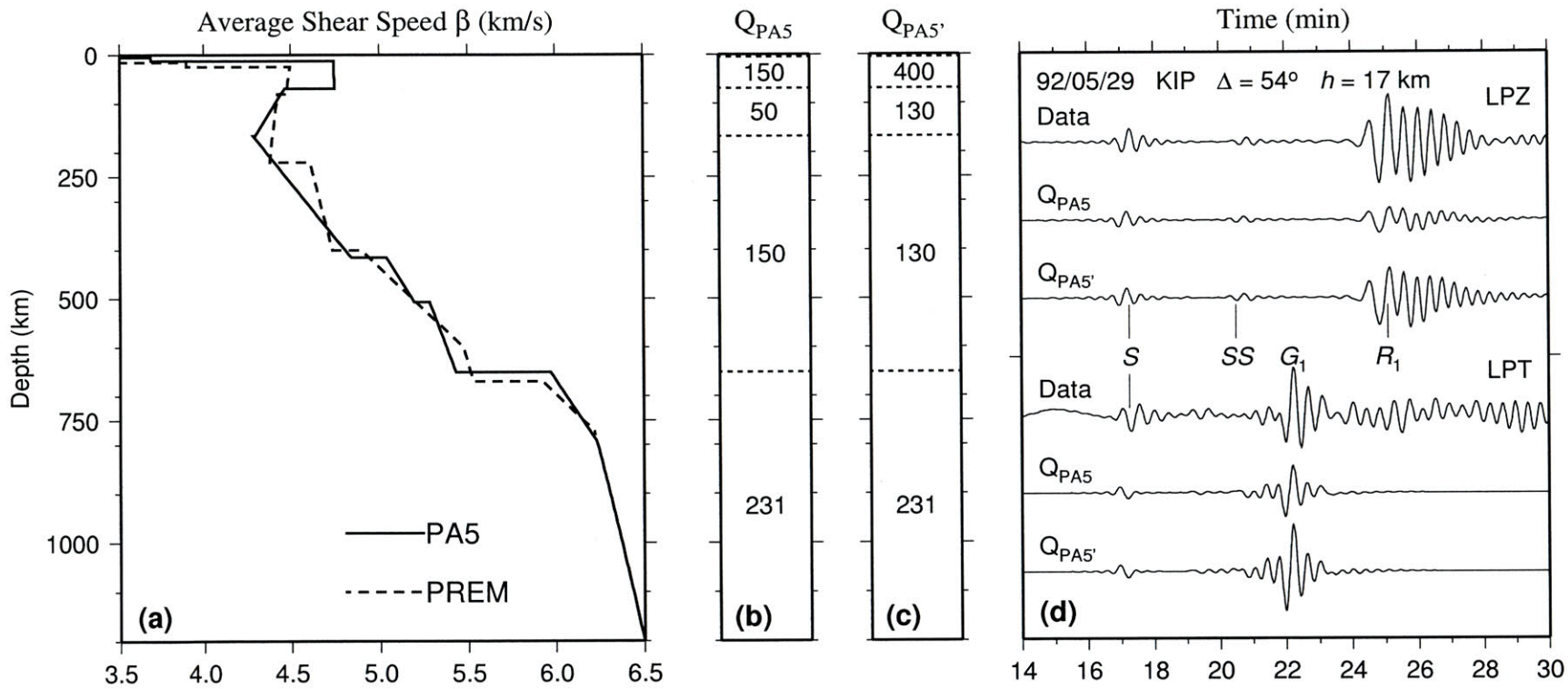
Average Shear Speed β (km/s)
Depth (km)
0
250
500
750
1000
3.5
4.0
4.5
5.0
5.5
6.0
6.5
PA5
PREM
(a)
Q_{PA5}
150
50
150
231
(b)
$Q_{PA5'}$
400
130
130
231
(c)
Time (min)
92/05/29 KIP Δ = 54° h = 17 km
Data
LPZ
Q_{PA5}
$Q_{PA5'}$
S
SS
G_1
R_1
LPT
Data
Q_{PA5}
$Q_{PA5'}$
(d)
14
16
18
20
22
24
26
28
30

Fig. 2

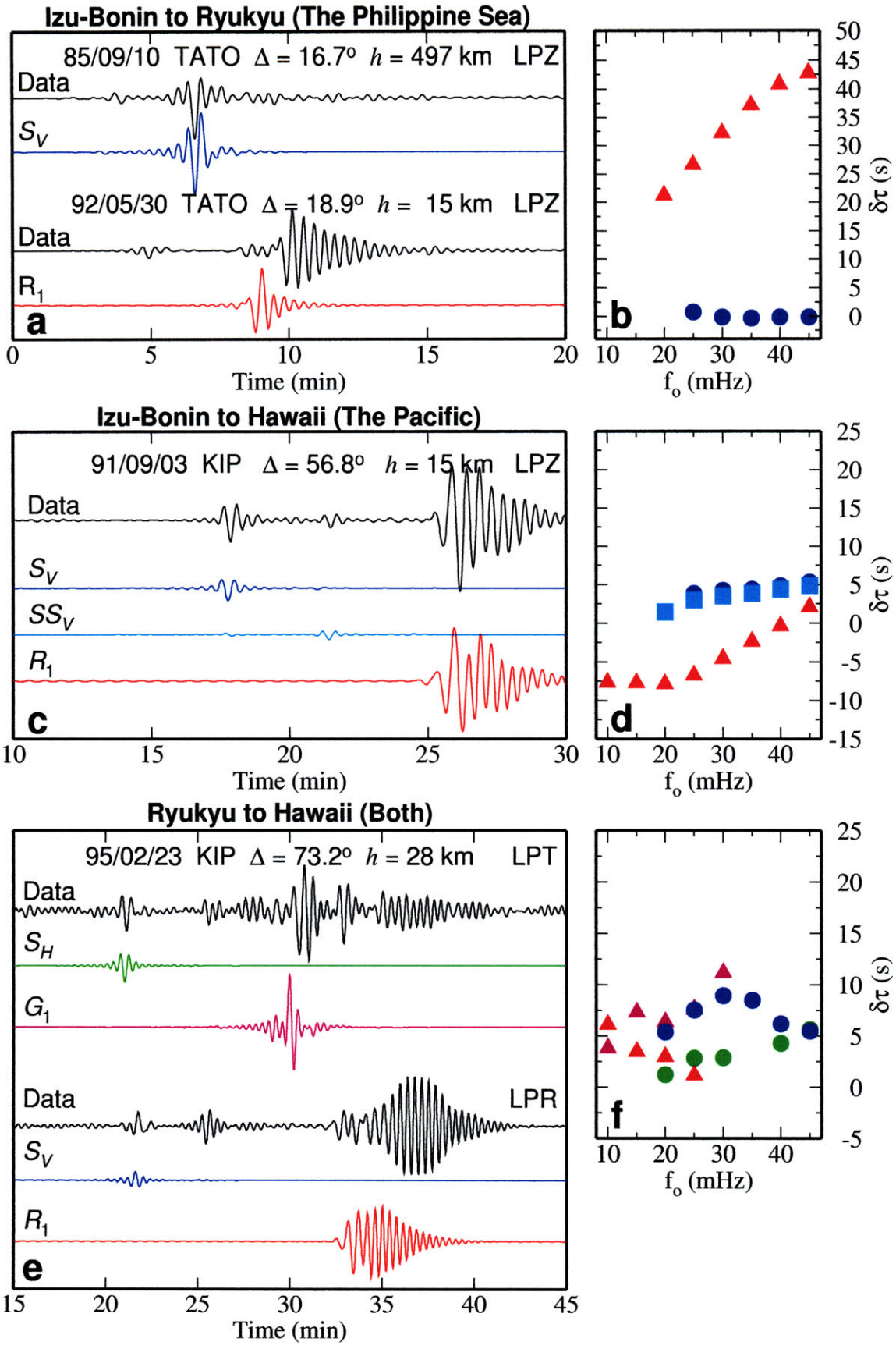
Izu-Bonin to Ryukyu (The Philippine Sea)
85/09/10 TATO Δ = 16.7° h = 497 km LPZ
Data
S_V
92/05/30 TATO Δ = 18.9° h = 15 km LPZ
Data
R_1
a
Time (min)
b
f_o (mHz)
δτ (s)
Izu-Bonin to Hawaii (The Pacific)
91/09/03 KIP Δ = 56.8° h = 15 km LPZ
Data
S_V
SS_V
R_1
c
Time (min)
d
f_o (mHz)
δτ (s)
Ryukyu to Hawaii (Both)
95/02/23 KIP Δ = 73.2° h = 28 km LPT
Data
S_H
G_1
Data
LPR
S_V
R_1
e
Time (min)
f
f_o (mHz)
δτ (s)

Fig. 3

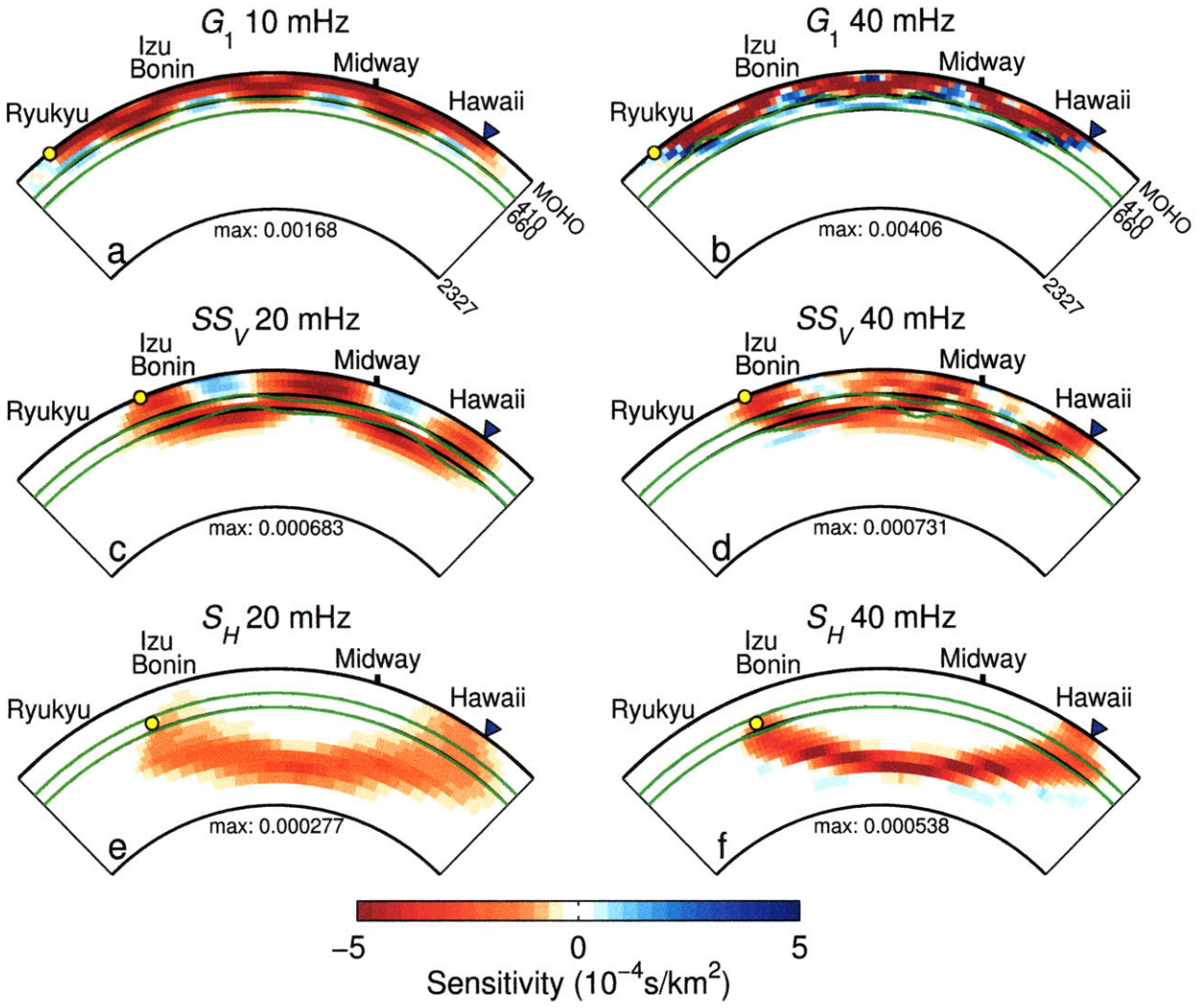
G_1 10 mHz
Izu
Bonin
Midway
Ryukyu
Hawaii
MOHO
410
660
2327
max: 0.00168
a
G_1 40 mHz
max: 0.00406
b
SS_V 20 mHz
max: 0.000683
c
SS_V 40 mHz
max: 0.000731
d
S_H 20 mHz
max: 0.000277
e
S_H 40 mHz
max: 0.000538
f
−5
0
5
Sensitivity (10^{-4}s/km^2)

Fig. 4

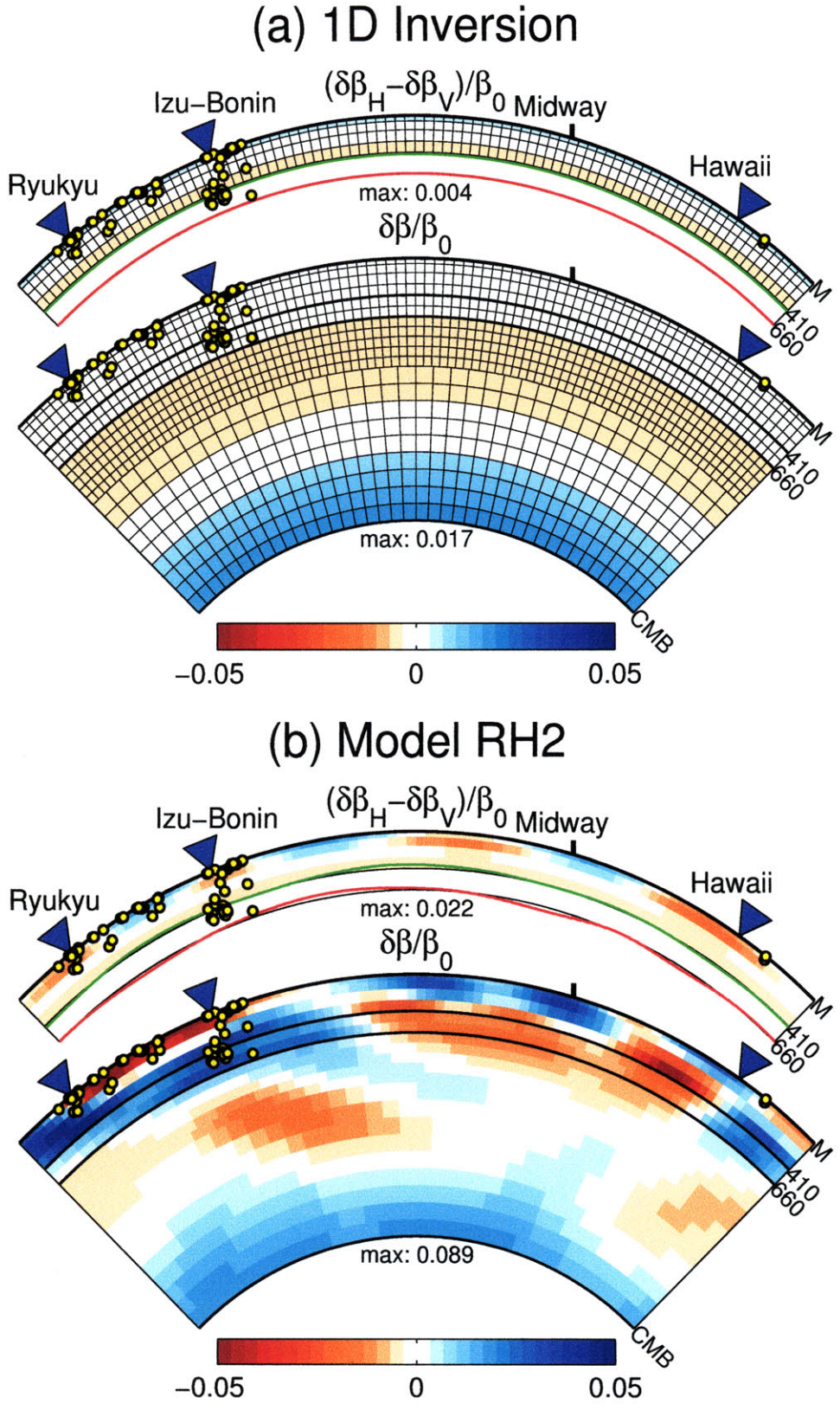
(a) 1D Inversion
$(\delta\beta_H - \delta\beta_V)/\beta_0$
Izu–Bonin
Midway
Ryukyu
Hawaii
max: 0.004
$\delta\beta/\beta_0$
M
410
660
max: 0.017
CMB
−0.05
0
0.05
(b) Model RH2
$(\delta\beta_H - \delta\beta_V)/\beta_0$
Izu–Bonin
Midway
Ryukyu
Hawaii
max: 0.022
$\delta\beta/\beta_0$
M
410
660
max: 0.089
CMB
−0.05
0
0.05

Fig. 5

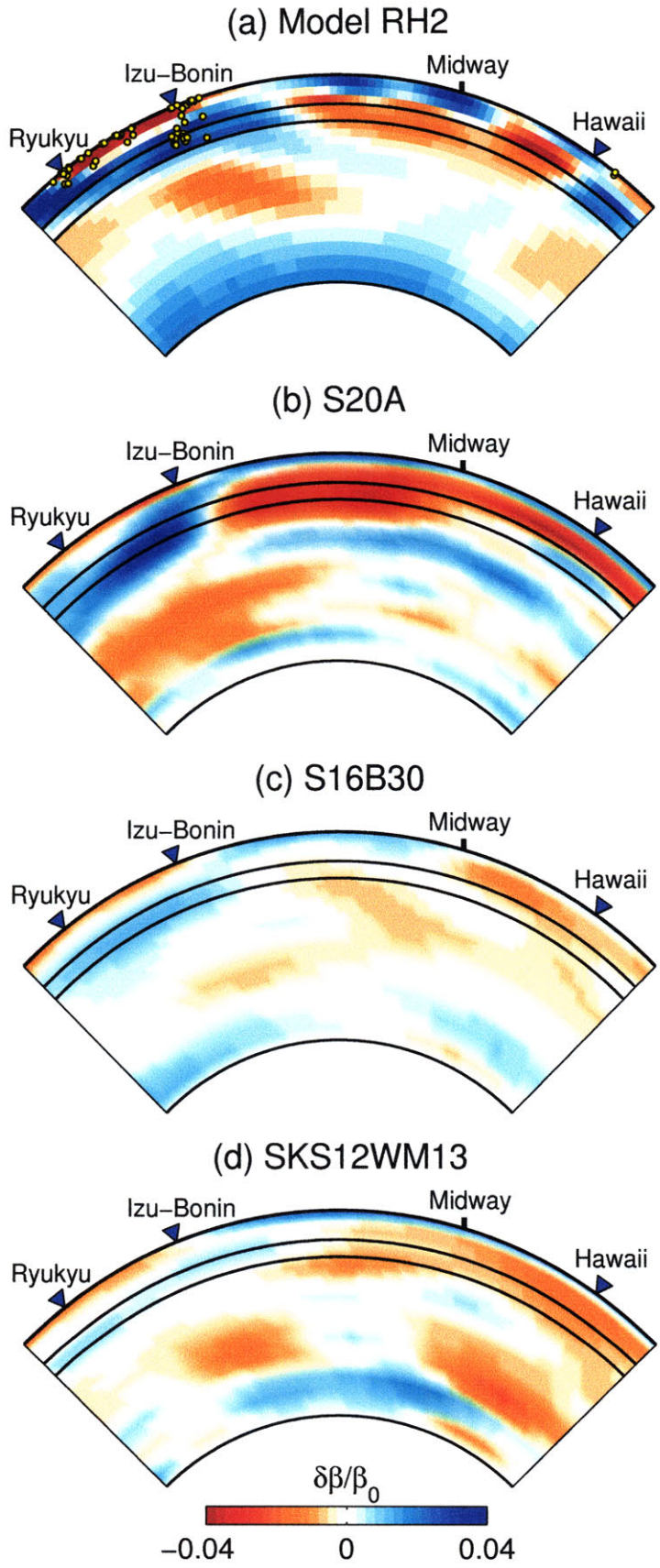
(a) Model RH2
Izu–Bonin
Midway
Ryukyu
Hawaii
(b) S20A
Izu–Bonin
Midway
Ryukyu
Hawaii
(c) S16B30
Izu–Bonin
Midway
Ryukyu
Hawaii
(d) SKS12WM13
Izu–Bonin
Midway
Ryukyu
Hawaii
δβ/β0
−0.04
0
0.04

Fig. 6

2D Inversion

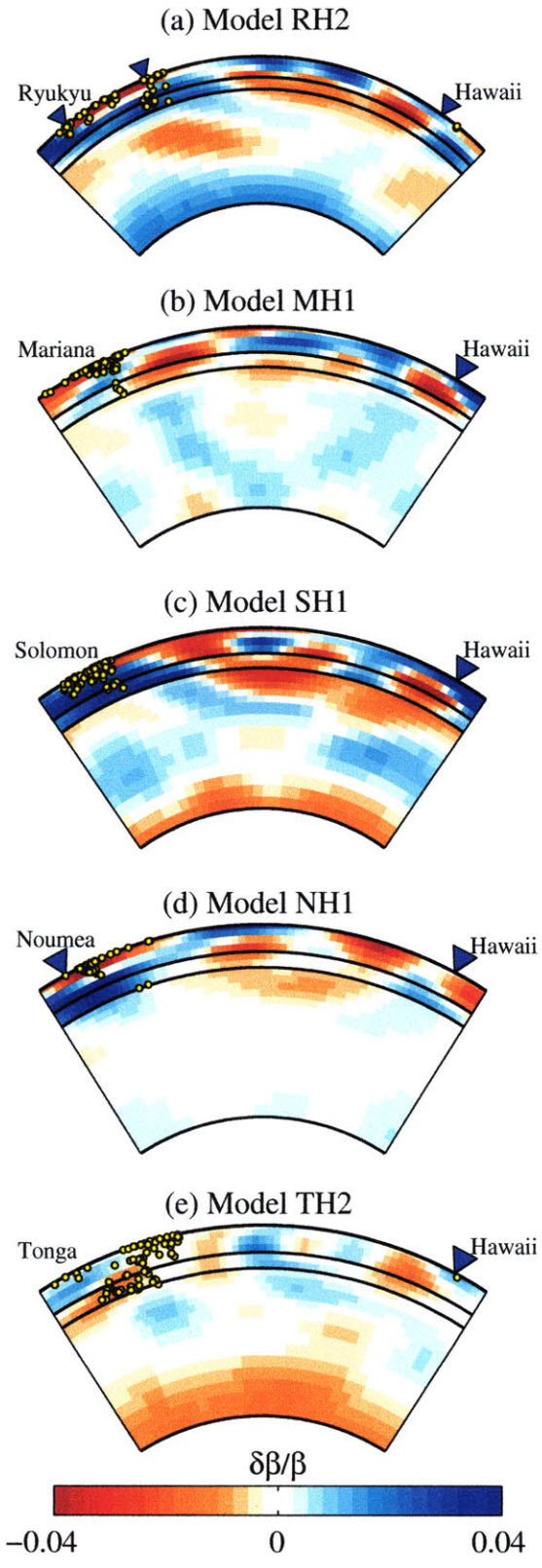

Fig. 7

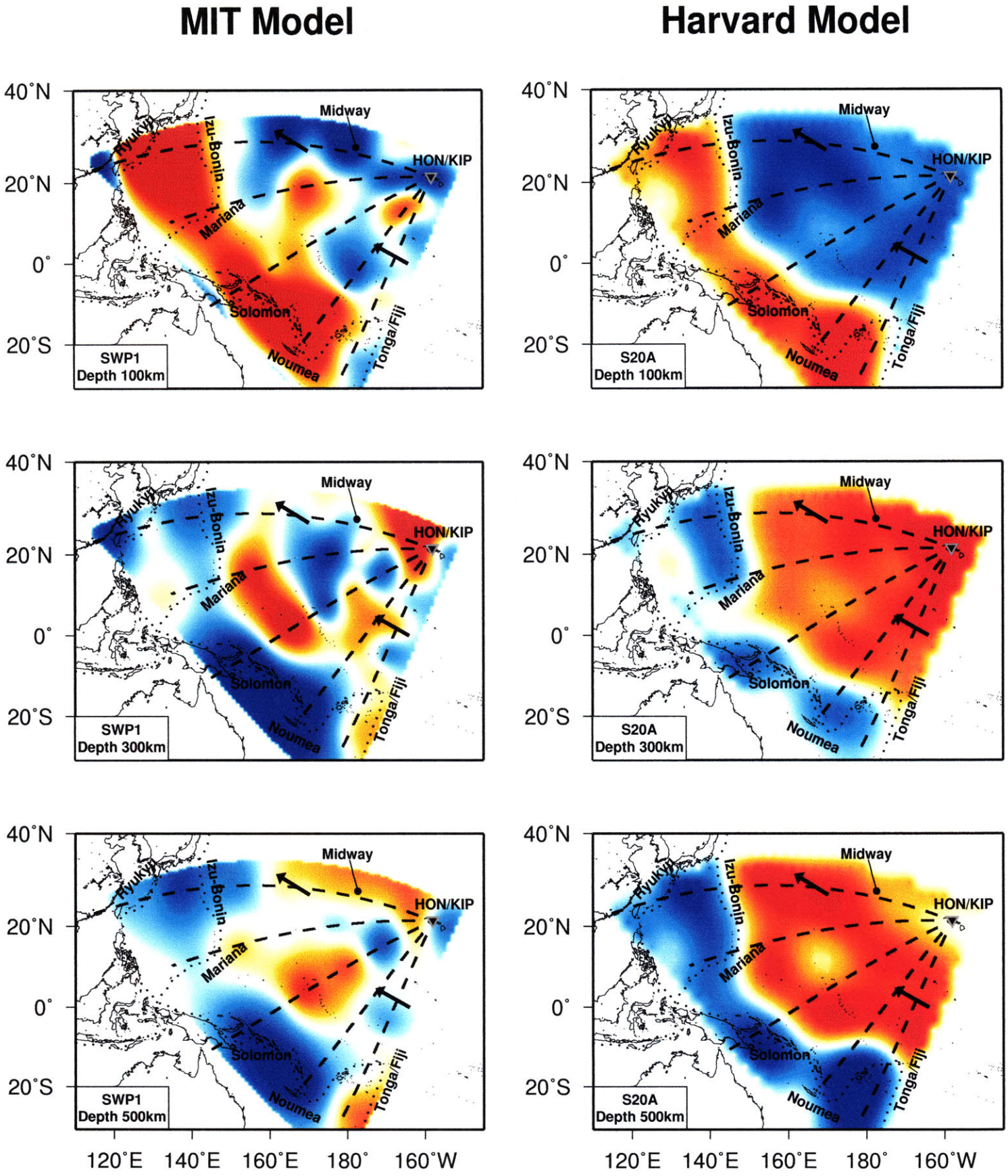
MIT Model
Harvard Model
40°N
20°N
0°
20°S
Midway
HON/KIP
Ryukyu
Izu-Bonin
Mariana
Solomon
Noumea
Tonga/Fiji
SWP1
Depth 100km
S20A
Depth 100km
SWP1
Depth 300km
S20A
Depth 300km
SWP1
Depth 500km
S20A
Depth 500km
120°E
140°E
160°E
180°
160°W

Fig. 8

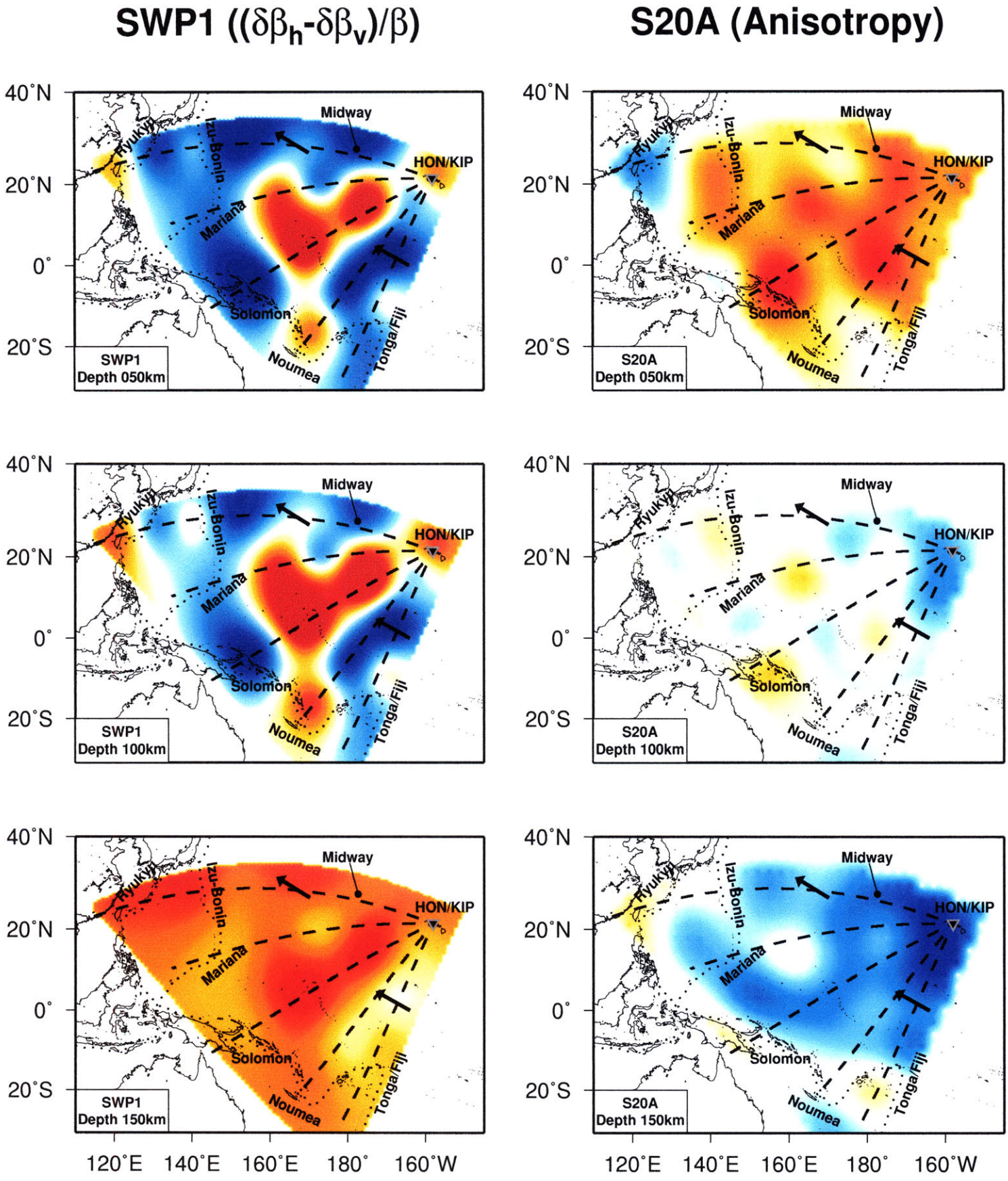
SWP1 ((δβh-δβv)/β)
S20A (Anisotropy)
40°N
20°N
0°
20°S
120°E
140°E
160°E
180°
160°W
Midway
HON/KIP
Ryukyu
Izu-Bonin
Mariana
Solomon
Noumea
Tonga/Fiji
SWP1 Depth 050km
S20A Depth 050km
SWP1 Depth 100km
S20A Depth 100km
SWP1 Depth 150km
S20A Depth 150km

Fig. 9

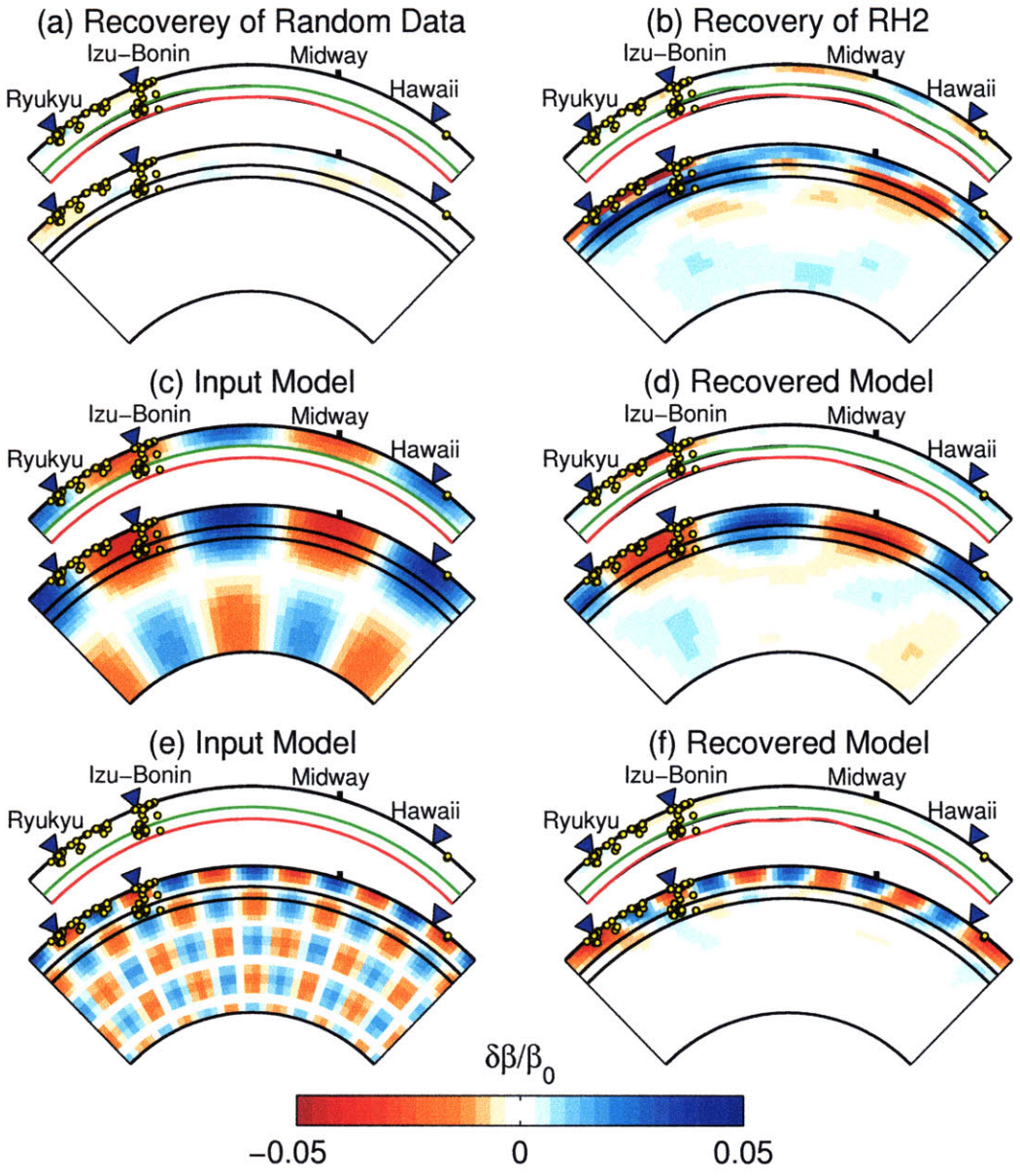
(a) Recoverey of Random Data
Izu–Bonin
Midway
Ryukyu
Hawaii
(b) Recovery of RH2
Izu–Bonin
Midway
Ryukyu
Hawaii
(c) Input Model
Izu–Bonin
Midway
Ryukyu
Hawaii
(d) Recovered Model
Izu–Bonin
Midway
Ryukyu
Hawaii
(e) Input Model
Izu–Bonin
Midway
Ryukyu
Hawaii
(f) Recovered Model
Izu–Bonin
Midway
Ryukyu
Hawaii
δβ/β0
−0.05
0
0.05

Fig. A1